

Quaternion Infrared Visible Image Fusion

Weihua Yang and Yicong Zhou, *Senior Member, IEEE*

Abstract—Visible images provide rich details and color information only under well-lighted conditions while infrared images effectively highlight thermal targets under challenging conditions such as low visibility and adverse weather. Infrared-visible image fusion aims to integrate complementary information from infrared and visible images to generate a high-quality fused image. Existing methods exhibit critical limitations such as neglecting color structure information in visible images and performance degradation when processing low-quality color-visible inputs. To address these issues, we propose a quaternion infrared-visible image fusion (QIVIF) framework to generate high-quality fused images completely in the quaternion domain. QIVIF proposes a quaternion low-visibility feature learning model to adaptively extract salient thermal targets and fine-grained texture details from input infrared and visible images respectively under diverse degraded conditions. QIVIF then develops a quaternion adaptive unsharp masking method to adaptively improve high-frequency feature enhancement with balanced illumination. QIVIF further proposes a quaternion hierarchical Bayesian fusion model to integrate infrared saliency and enhanced visible details to obtain high-quality fused images. Extensive experiments across diverse datasets demonstrate that our QIVIF surpasses state-of-the-art methods under challenging low-visibility conditions.

Index Terms—Quaternion infrared visible image fusion, quaternion low-rank decomposition, quaternion unsharp masking.

I. INTRODUCTION

Infrared-visible image fusion (IVIF) techniques enable complementary features of infrared and visible images to be combined into a fused image. It significantly facilitates subsequent applications such as object detection [1], [2], target tracking [3], [4] and biometric recognition [5], [6]. As seen in Fig. 1, visible images exhibit reflection information while infrared imaging captures the thermal radiation of targets and low-texture background without the negative impacts of atmospheric light.

Existing IVIF methods can be broadly categorized into traditional model-based and deep-learning-based ones. Recent advances in deep-learning-based methods leverage diverse architectures including generative adversarial networks [7], [8], and vision transformers [9]. They have achieved competitive performance. However, these deep-learning-based IVIF methods focus on preserving illumination-based thermal saliency in infrared images while ignoring color structure and details in the visible images [10]. For instance, when processing visible images, many deep-learning-based IVIF methods [11],

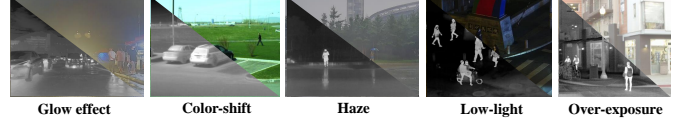


Fig. 1. Samples pairs of the infrared and the visible from the challenging low-visibility scenarios including glow effects, color shifts, haze, low light and over-exposure conditions.

[12] convert RGB images into YCbCr space and retain only the luminance (Y) channel for image fusion while discarding chrominance (Cb/Cr) channels during feature extraction and fusion. This transformation inherently neglects cross-channel interactions and often results in fused images with color casts or desaturation [10]. To circumvent degraded scenarios, recent deep-learning-based IVIF methods adopt auxiliary task-guided learning by integrating illumination-based enhancement modules [11], [13] to enhance feature extraction and fused images with task-specific priors. However, their fused images often exhibit obscured critical details that hinder human perception. As seen in Fig. 2, despite high saliency in fused images, deep-learning-based methods fail to effectively maintain fine-grained details of visible images.

On the other hand, traditional model-based IVIF methods are inherently training-free, bypassing the need for data-driven feature representation learning. However, traditional model-based IVIF methods are predominantly designed for fusing single-channel infrared and grayscale visible image pairs. When applied to color visible images, traditional model-based methods often rely on channel-wise fusion strategies that treat each color channel as a grayscale image and fuse them with the infrared one-by-one. For example, [14] designed a two-scale decomposition model to obtain the base (low-frequency) and detail (high-frequency) layers from grayscale pairs. It independently fuses these layers across infrared and visible images via heuristic rules and generates fused images channel-by-channel [15]. The fused color image is synthesized by concatenating three independently fused channels. Such channel-wise processing fails to consider cross-channel interactions of color images and leads to color distortion [16]. Traditional IVIF methods leverage multi-scale feature extraction and fusion (e.g., edge-preserving filters, gradient operators, low-rank representation) to enhance edges and gradients common to both infrared and visible images [14], [17], [18]. However, these methods insufficiently adapt to the modality-specific characteristics of the infrared and visible images and may result in insufficient or redundant feature enhancement as seen in Fig. 2. Traditional methods struggle to disentangle scenario-specific details from degraded visible

This work was funded by the Science and Technology Development Fund, Macau SAR (File no. 0049/2022/A1, 0050/2024/AGJ), by the University of Macau (File no. MYRG-GRG2024-00181-FST). (Corresponding author: Yicong Zhou.)

Weihua Yang and Yicong Zhou are with the Department of Computer and Information Science, University of Macau, Macau 999078, China. (e-mail: weihuayang.um@gmail.com; yicongzhou@um.edu.mo)



Fig. 2. Visual Comparison of various IVIF algorithms in normal and low visibility conditions. VIS denotes the visible images. LatLRR [17] and AVSHB [14] correspond to traditional model-based IVIF methods. SHIP [12] and DAFusion [13] are deep-learning-based methods. Compared to deep-learning-based methods, LatLRR and AVSHB inject more grayscale pixels of the infrared and exhibit a low-contrast background particular in the low-visibility condition.

images and often overcompensate by fusing redundant thermal information into the fused images [11]. This imbalance leads to low-visibility where fused images exhibit obvious shadows, washed-out textures or loss of chromatic fidelity for human perception (see Fig. 2).

Quaternion representation is an effective tool for color image processing, encoding a color image as a pure quaternion matrix. It preserves the inter-relationships between the red, green, and blue channels of color images [19], [20] and fully utilizes the highly correlated color information. This provides better performance compared to real-valued methods [21]. Specifically, quaternion-based low-rank regularization leverages the algebraic properties of quaternions while enforcing low-rank constraints. This approach has been widely applied in various color image processing tasks, such as color image recovery [22], color image denoising [23], and color image stitching [24]. Furthermore, [25] demonstrated that quaternion representation enhances the exploration of low-rank properties and provides superior quality performance.

Taking advantage of the quaternion representation, this paper introduces a unified quaternion infrared visible fusion framework to simultaneously address the above fusion challenges. Our main contributions are presented as follows:

- We propose a quaternion image fusion (QIVIF) framework to address multiple low-contrast scenarios (e.g., glow effect, color-shift, haze, low-light and over-exposure). To the best knowledge, our QIVIF is the first to perform infrared and visible image fusion **completely in the quaternion domain**.
- QIVIF proposes a unified quaternion low-visibility feature learning model to adaptively disentangle infrared saliency (thermal targets) and visible details (textures, edges) while preserving highly correlated color information under diverse low-visibility scenarios.
- QIVIF develops a quaternion adaptive unsharp masking method to obtain a promising detail-enhanced visible image with balanced illumination. We are the first to bring the unsharp masking concept to the quaternion domain for color image enhancement.
- QIVIF proposes a quaternion hierarchical Bayesian fusion model to integrate infrared saliency and enhanced visible details using adaptive feature weighting. This en-

sures trade-offs between high saliency of thermal targets and high visibility for human perception in fused images.

- Extensive experiments on various datasets demonstrate that our QIVIF outperforms the state-of-the-art methods.

The rest of this paper is organized as follows: Section II presents the preliminaries of quaternion representation. Section III introduces our framework in detail. Section IV presents the experiments and comparisons. Finally, Section V gives the conclusions.

II. PRELIMINARIES

Quaternions provide a holistic color image processing by encapsulating color channels within a single algebraic structure. Below is a detailed introduction to quaternion algebra and its application in color image representation.

A. Quaternion algebra and representation

A quaternion scalar denoted as $\dot{q} \in \mathbb{H}$ is a hypercomplex number with one real part and three imaginary parts. It is defined as $\dot{q} = a + b\mathbf{i} + c\mathbf{j} + d\mathbf{k}$, where $a, b, c, d \in \mathbb{R}$ and $\mathbf{i}, \mathbf{j}, \mathbf{k}$ are imaginary units satisfying: $\mathbf{i}^2 = \mathbf{j}^2 = \mathbf{k}^2 = \mathbf{i}\mathbf{j}\mathbf{k} = -1$.

Quaternion addition and subtraction follow a component-wise rule as that in the complex space. However, quaternion multiplication is generally non-commutative and the multiplication rule is defined as $\mathbf{i}\mathbf{j} = -\mathbf{j}\mathbf{i} = \mathbf{k}$, $\mathbf{j}\mathbf{k} = -\mathbf{k}\mathbf{j} = \mathbf{i}$, $\mathbf{k}\mathbf{i} = -\mathbf{i}\mathbf{k} = \mathbf{j}$. Quaternion conjugate and modulus are key operations defined below,

$$\bar{\dot{q}} = a - b\mathbf{i} - c\mathbf{j} - d\mathbf{k}, |\dot{q}| = \sqrt{a^2 + b^2 + c^2 + d^2}.$$

B. Quaternion representation

Quaternions provide mathematically elegant color image processing by unifying RGB channels into a single hypercomplex entity. For color image representation, each color pixel q with its RGB values (r, g, b) is encoded as a pure quaternion scalar $\dot{q} = r\mathbf{i} + g\mathbf{j} + b\mathbf{k}$. As shown in Fig. 3, three color channels of a color image \mathbf{A} are represented as two-dimensional pure quaternion matrix $\dot{\mathbf{A}}$.

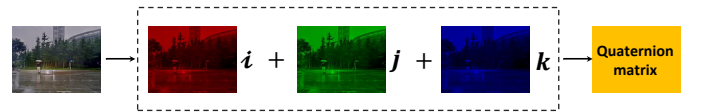


Fig. 3. Quaternion representation of a color image. We encode the three channels of the color image into a pure quaternion matrix.

For a quaternion matrix $\dot{\mathbf{A}} \in \mathbb{H}^{H \times W}$ with each element denoted as $\dot{a}_{i,j}$, its conjugate transpose is denoted as $\dot{\mathbf{A}}^H = (\bar{\dot{a}}_{j,i}) \in \mathbb{H}^{W \times H}$. The ℓ_1 and Frobenius norms are computed as $\|\dot{\mathbf{A}}\|_1 = \sum_{i=1}^H \sum_{j=1}^W |\dot{a}_{i,j}|$, $\|\dot{\mathbf{A}}\|_F = (\sum_{i=1}^H \sum_{j=1}^W |\dot{a}_{i,j}|^2)^{\frac{1}{2}}$.

Spatial derivatives in x and y directions can be computed in the quaternion domain. The gradient magnitude combines information from all channels to produce consistent color edges. The first-order quaternion gradients [26] can be defined as $\frac{\partial \dot{\mathbf{I}}}{\partial x}$ and $\frac{\partial \dot{\mathbf{I}}}{\partial y}$ at a vertical or horizontal direction. The second-order gradients can be defined as $\frac{\partial^2 \dot{\mathbf{I}}}{\partial^2 x}$, $\frac{\partial^2 \dot{\mathbf{I}}}{\partial^2 y}$ and $\frac{\partial^2 \dot{\mathbf{I}}}{\partial x \partial y}$.

C. Quaternion low rank regularization

Let a quaternion matrix $\dot{\mathbf{X}} \in \mathbb{H}^{H \times W}$ be constrained to a low-rank structure. To approximate its solution, the quaternion nuclear norm as a convex surrogate for rank minimization is defined as $\|\dot{\mathbf{X}}\|_* = \sum_i^r \sigma_i(\dot{\mathbf{X}})$ where $\sigma_i(\dot{\mathbf{X}})$ denote the real non-negative singular values of $\dot{\mathbf{X}}$ obtained from quaternion singular value decomposition (QSVD) [27]. QSVD factorizes $\sigma_i(\dot{\mathbf{X}})$ into quaternion-valued unitary matrices and a diagonal matrix of real singular values.

However, the quaternion nuclear norm often yields suboptimal rank approximations due to its uniform penalization of all singular values [28]. To address this, weighted Schatten- p norm and partial sum of singular values are extended to the quaternion domain.

Lemma 1. (Quaternion weighted Schatten- p norm [19]) For any $\lambda \geq 0$, quaternion matrix $\dot{\mathbf{Y}}$ and $\dot{\mathbf{X}} \in \mathbb{H}^{H \times W}$ with the rank of r , then the quaternion weighted Schatten p -norm problem ($0 < p < 1$) can be defined as:

$$\arg \min_{\dot{\mathbf{X}}} \frac{1}{2} \|\dot{\mathbf{Y}} - \dot{\mathbf{X}}\|_F^2 + \lambda \|\dot{\mathbf{X}}\|_{w, S_p}^p, \quad (1)$$

with the given p and w , there exists a specific threshold ($p < 1$) $\tau_p^{GST}(\lambda w) = (2\lambda w(1-p))^{\frac{1}{2-p}} + \lambda w p(2\lambda w(1-p))^{\frac{p-1}{2-p}}$. Then we have two conclusions. (1) When $\sigma_i(\dot{\mathbf{Y}}) \leq \tau_p^{GST}(\lambda w)$, the optimal solution of equation (1) is $\sigma_i(\dot{\mathbf{X}}) = 0$. (2) When $\sigma_i(\dot{\mathbf{Y}}) > \tau_p^{GST}(\lambda w)$, the optimal solution of equation (1) is $\sigma_i(\dot{\mathbf{X}}) - \sigma_i(\dot{\mathbf{Y}}) + \lambda w p(\sigma_i(\dot{\mathbf{X}}))^{p-1}$.

Lemma 2. (Quaternion partial sum of singular values [29]) For any $\lambda \geq 0$, quaternion matrix $\dot{\mathbf{Y}}$ and $\dot{\mathbf{X}} \in \mathbb{H}^{H \times W}$ with the rank of r , then the minimization problem of the partial sum of quaternion singular values can be defined as:

$$\arg \min_{\dot{\mathbf{X}}} \frac{1}{2} \|\dot{\mathbf{Y}} - \dot{\mathbf{X}}\|_F^2 + \lambda \|\dot{\mathbf{X}}\|_{p=n} \quad (2)$$

the closed form solution of this equation is $\dot{\mathbf{U}}_1 \Sigma_1 \dot{\mathbf{V}}_1^H + \dot{\mathbf{U}}_2 S_\lambda(\Sigma_2) \dot{\mathbf{V}}_2^H$ using QSVD of $\dot{\mathbf{Y}}$, where Σ_1 is a diagonal real matrix with singular values $\text{diag}(\sigma_1, \sigma_2, \dots, \sigma_n)$, Σ_2 is a diagonal real matrix with singular values $\text{diag}(\sigma_{n+1}, \sigma_{n+2}, \dots, \sigma_r)$ and $S_\lambda(\cdot)$ denotes the soft thresholding operator with parameter λ .

III. PROPOSED FRAMEWORK

A. Overview

Our quaternion infrared visible image fusion (QIVIF) framework proposes a pixel-level feature extraction and fusion pipeline as illustrated in Fig. 4. To holistically model the cross-channel relationships within a color visible image, QIVIF first encodes visible and infrared images as pure quaternion matrices using quaternion representation. The three RGB channels of the visible image are mapped to the three imaginary components of a quaternion matrix to preserve high-correlated color information. The single-channel infrared image is replicated across three dimensions to construct a compatible quaternion structure. This enables unified feature representation of both modalities within a shared framework.

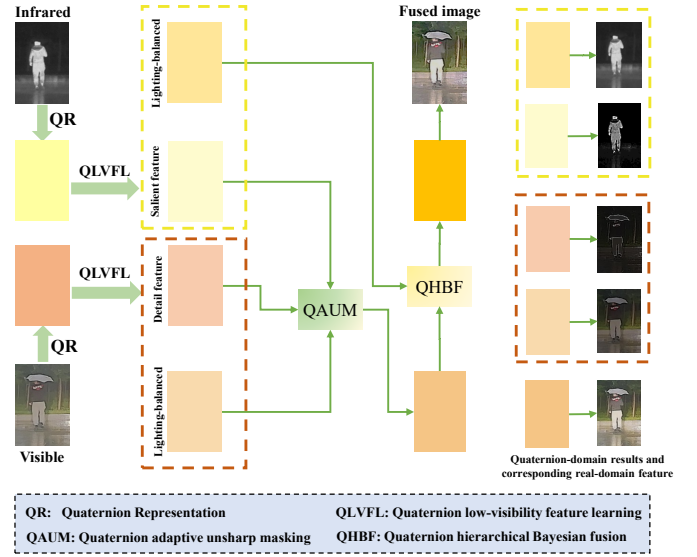


Fig. 4. Flowchart of our quaternion infrared visible image fusion.

To address feature extraction under diverse low-visibility scenarios, QIVIF introduces a unified quaternion low-visibility feature learning model. This model derives lighting-suppressed quaternion representations and disentangles modality-specific features for the infrared and visible quaternion representations respectively. Furthermore, QIVIF proposes a quaternion adaptive unsharp masking method to enhance fine-grained details and target saliency and reconstruct a sharpened visible quaternion representation with balanced illumination inspired by [30]. Finally, QIVIF introduces a quaternion hierarchical Bayesian fusion model to merge the sharpened visible and lighting-suppressed infrared quaternion representations. This model effectively generates fused images with critical image details and high-contrast visibility.

B. Quaternion low-visibility feature learning

To handle degraded color-visible images and learn modality-specific features for both infrared and visible images, this subsection proposes a unified quaternion low-visibility feature learning (QLVFL) model. It consists of a quaternion lighting suppression module to remove various degradation effects and a quaternion low-rank decomposition module to learn the thermal saliency and fine-grained image details for infrared and visible images respectively.

1) *Quaternion lighting suppression:* Visible images primarily capture reflected light and offer an intuitive representation of objects with abundant details. However, they are limited in overcoming environmental disturbances [14]. The quaternion lighting suppression (QLS) module aims to eliminate the negative impacts of diverse degraded effects including glow effects, color shifts, haze, low-light and overexposure conditions. This module assumes that the low-quality image can be decomposed into a low-illumination layer and an over-smooth and bright layer representing the negative impacts of the scene.

$$\dot{\mathbf{L}}(x) = \dot{\mathbf{I}}(x) + \dot{\mathbf{G}}(x);$$

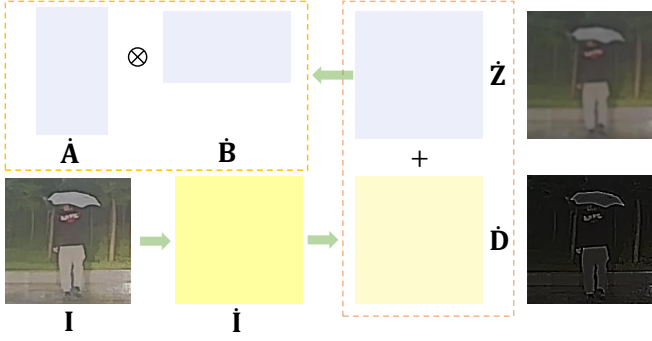


Fig. 5. Decomposition results of the infrared and the visible using QLRD model. The QLRD model decomposes the given input quaternion representation into a smooth structure feature layer and a salient target feature layer with rich details.

Considering the brightness decreases gradually and smoothly, we exploit this smoothness attribute and employ the method of target layer separation for scenes where one layer is significantly smoother than the other [31]. The core is to remove the bright regions with low gradients and retain large gradients for the separated layer $\hat{\mathbf{I}}$. The formulation is presented as follows:

$$\begin{aligned} \arg \min_{\hat{\mathbf{I}}} \quad & \|H(\nabla \hat{\mathbf{I}})\|_1 + \lambda \|\Delta \hat{\mathbf{I}} - \Delta \hat{\mathbf{I}}\|_F^2, \\ \text{s.t.} \quad & 0 \leq b(\hat{\mathbf{I}}) \leq b(\hat{\mathbf{I}}), \hat{\mathbf{G}} = H(\nabla \hat{\mathbf{I}}) \end{aligned} \quad (3)$$

where ∇ denotes the first-order gradient filter, and Δ denotes the second-order gradient filter. $b(\hat{\mathbf{I}})$ is a function to extract the intensity component of quaternion matrix $\hat{\mathbf{I}}$ (see details in supplementary material). The function $H(\hat{\mathbf{I}})$ is to minimize the small values of $\hat{\mathbf{I}}$ as following equation:

$$H(\hat{\mathbf{X}})(s, t) = \begin{cases} \hat{\mathbf{X}}(s, t), & \|\hat{\mathbf{X}}(s, t)\| > \tau \\ 0, & \text{otherwise.} \end{cases} \quad (4)$$

2) *Quaternion low-rank decomposition:* Given an observed three-dimensional matrix $\mathbf{I} \in \mathbb{R}^{H \times W \times 3}$ (i.e., a visible image) and its quaternion representation can be denoted as $\hat{\mathbf{I}}$. For the infrared image $\mathbf{I}_f \in \mathbb{R}^{H \times W}$, we first replicate the grayscale channel to construct a three-dimensional matrix then we apply the quaternion representation in the new infrared image with the same three channels. Considering the smooth property in the background area and sparsity of the detail layer, we propose a quaternion low-rank decomposition module (QLRD). It is assumed to be decomposed into a structure layer $\hat{\mathbf{Z}}$ and a detail layer $\hat{\mathbf{D}}$ with weighted low rank prior as.

$$\begin{aligned} \arg \min_{\hat{\mathbf{Z}}, \hat{\mathbf{D}}} \quad & \|\hat{\mathbf{Z}}\|_{w, S_p, p_1=n}^p + \beta \|\hat{\mathbf{D}}\|_1 + \gamma \|\hat{\mathbf{D}}\|_F^2 \\ \text{s.t.} \quad & \hat{\mathbf{I}} = \hat{\mathbf{Z}} + \hat{\mathbf{D}} + \hat{\mathbf{E}}, \end{aligned} \quad (5)$$

where $\hat{\mathbf{Z}} \in \mathbb{H}^{H \times W}$ is constrained in quaternion weighted Schatten p -norm and weighted diagonal matrix \mathbf{W} . To better relax $\hat{\mathbf{Z}}$ in this nonconvex term, the partial sum of singular values is utilized to minimize residual rank when $p_1 > n$. Since the non-convex surrogate for the rank function, the Schatten- p norm with $0 < p < 1$ makes a closer approximation to the rank function than the nuclear norm.

Lemma 3. (Quaternion singular value inequality of bilinear factorization [19]) Let two quaternion matrices $\hat{\mathbf{X}} \in \mathbb{H}^{H \times r}$ and $\hat{\mathbf{Y}} \in \mathbb{H}^{r \times W}$ be given and let $p > 0$. K is denoted as $\min(H, W, r)$. The inequality holds for the decreasingly ordered singular values of $\hat{\mathbf{X}}$, $\hat{\mathbf{Y}}$ and $\hat{\mathbf{X}}\hat{\mathbf{Y}}$.

$$\sum_k^K \sigma_k^p(\hat{\mathbf{X}}\hat{\mathbf{Y}}) \leq \sum_k^K \sigma_k^p(\hat{\mathbf{X}}) \sigma_k^p(\hat{\mathbf{Y}}) \quad (6)$$

where $\sigma_k(\hat{\mathbf{X}})$ is the k -th singular value of $\hat{\mathbf{X}}$.

Inspired by [19], for $\hat{\mathbf{Z}} \in \mathbb{H}^{H \times W}$, it is constrained with rank $r < \min(H, W)$ and can be decomposed into two smaller quaternion factor matrices $\hat{\mathbf{A}} \in \mathbb{H}^{H \times r}$ and $\hat{\mathbf{B}} \in \mathbb{H}^{r \times W}$ such that $\hat{\mathbf{Z}} = \hat{\mathbf{A}}\hat{\mathbf{B}}$. Lemma 3 allows us to make a factorization of larger quaternion matrices for arbitrary p quasi-norm.

Based on this, we develop a new inequality of bilinear factorization under quaternion weighted Schatten p -norm in the following Theorem 1.

Theorem 1. Let a quaternion matrix $\hat{\mathbf{X}} \in \mathbb{H}^{h \times w}$ and a diagonal weight matrix \mathbf{W} be given, then the decomposed quaternion matrices $\hat{\mathbf{A}} \in \mathbb{H}^{h \times r}$ and $\hat{\mathbf{B}} \in \mathbb{H}^{r \times w}$ can be obtained. Let $p > 0$. K is denoted as $\min(H, W, r)$. The following inequality holds for the decreasingly ordered singular values of $\hat{\mathbf{A}}$, $\hat{\mathbf{B}}$ and $\hat{\mathbf{X}}$.

$$\sum_k^K \mathbf{W}_k \sigma_k^p(\hat{\mathbf{X}}) \leq \frac{1}{2} \sum_k^K \mathbf{W}_{1,k}^2 \sigma_k^{2p}(\hat{\mathbf{A}}) + \frac{1}{2} \sum_k^K \mathbf{W}_{2,k}^2 \sigma_k^{2p}(\hat{\mathbf{B}}) \quad (7)$$

where \mathbf{W} is the multiplication results of \mathbf{W}_1 and \mathbf{W}_2 .

The proof of Theorem 1 can be found in the supplementary material.

3) *Overall model formulation:* Considering the effectiveness of the bilinear factor matrix norm [19], [32], the Eq. (5) is reformulated as follows according to the Theorem 1:

$$\begin{aligned} \arg \min_{\hat{\mathbf{A}}, \hat{\mathbf{B}}, \hat{\mathbf{D}}} \quad & \|\hat{\mathbf{A}}\|_{w, S_p, p_1=n}^p + \|\hat{\mathbf{B}}\|_{w, S_p, p_1=n}^p + \beta \|\hat{\mathbf{D}}\|_1 + \gamma \|\hat{\mathbf{D}}\|_F^2 \\ \text{s.t.} \quad & \hat{\mathbf{I}} = \hat{\mathbf{Z}} + \hat{\mathbf{D}} + \hat{\mathbf{E}}, \hat{\mathbf{Z}} = \hat{\mathbf{A}}\hat{\mathbf{B}} \end{aligned} \quad (8)$$

where $\hat{\mathbf{A}} \in \mathbb{H}^{H \times r}$ and $\hat{\mathbf{B}} \in \mathbb{H}^{r \times W}$ have the same rank r to reduce the computation complexity of single factor $\hat{\mathbf{Z}}$. The objective function of our unified quaternion low-contrast feature learning model is defined in the following by integrating Eqs. (3) and (8):

$$\begin{aligned} \arg \min_{\hat{\mathbf{A}}, \hat{\mathbf{B}}, \hat{\mathbf{D}}} \quad & \alpha \|\hat{\mathbf{A}}\|_{w, S_p, p_1=n}^p + \alpha \|\hat{\mathbf{B}}\|_{w, S_p, p_1=n}^p + \beta \|\hat{\mathbf{D}}\|_1 \\ & + \gamma \|\hat{\mathbf{D}}\|_F^2 + \|H(\nabla \hat{\mathbf{I}})\|_1 + \lambda \|\Delta \hat{\mathbf{I}} - \Delta \hat{\mathbf{J}}\|_F^2 \\ \text{s.t.} \quad & 0 \leq b(\hat{\mathbf{I}}) \leq b(\hat{\mathbf{J}}), \hat{\mathbf{G}} = H(\nabla \hat{\mathbf{I}}) \\ & \hat{\mathbf{I}} = \hat{\mathbf{Z}} + \hat{\mathbf{D}} + \hat{\mathbf{E}}, \hat{\mathbf{Z}} = \hat{\mathbf{A}}\hat{\mathbf{B}} \end{aligned} \quad (9)$$

4) *Optimization:* We adopt the linearized alternating direction method with adaptive penalty (LADMAP) methods in

the quaternion domain and convert (8) using the quaternion ADMM framework [33] as follows:

$$\begin{aligned} \mathcal{L} = & \alpha \|\dot{\mathbf{J}}\|_{w, S_p, p_1=n}^p + \frac{\mu_1}{2} \|\dot{\mathbf{A}} - \dot{\mathbf{J}}\|_F^2 + \langle \dot{\mathbf{Y}}_3, \dot{\mathbf{A}} - \dot{\mathbf{J}} \rangle \\ & + \alpha \|\dot{\mathbf{P}}\|_{w, S_p, p_1=n}^p + \frac{\mu_1}{2} \|\dot{\mathbf{B}} - \dot{\mathbf{P}}\|_F^2 + \langle \dot{\mathbf{Y}}_4, \dot{\mathbf{B}} - \dot{\mathbf{P}} \rangle \\ & + \langle \dot{\mathbf{Y}}_2, \dot{\mathbf{Z}} - \dot{\mathbf{A}}\dot{\mathbf{B}} \rangle + \frac{\mu_1}{2} \|\dot{\mathbf{Z}} - \dot{\mathbf{A}}\dot{\mathbf{B}}\|_F^2 + \beta \|\dot{\mathbf{D}}\|_1 \\ & + \gamma \|\dot{\mathbf{E}}\|_F^2 + \langle \dot{\mathbf{Y}}_1, \dot{\mathbf{I}} - \dot{\mathbf{Z}} - \dot{\mathbf{D}} - \dot{\mathbf{E}} \rangle \\ & + \frac{\mu_1}{2} \|\dot{\mathbf{I}} - \dot{\mathbf{Z}} - \dot{\mathbf{D}} - \dot{\mathbf{E}}\|_F^2 + \|\dot{\mathbf{G}}\|_1 + \lambda \|\Delta \dot{\mathbf{I}} - \Delta \dot{\mathbf{L}}\|_F^2 \\ & + \langle \dot{\mathbf{Y}}_5, \dot{\mathbf{G}} - H(\nabla \dot{\mathbf{I}}) \rangle + \frac{\mu_2}{2} \|\dot{\mathbf{G}} - H(\nabla \dot{\mathbf{I}})\|_F^2, \\ \text{s.t. } & 0 \leq b(\dot{\mathbf{I}}) \leq b(\dot{\mathbf{L}}) \end{aligned} \quad (10)$$

where $\dot{\mathbf{Y}}_1 \in \mathbb{H}^{H \times W}$, $\dot{\mathbf{Y}}_2 \in \mathbb{H}^{H \times W}$, $\dot{\mathbf{Y}}_5 \in \mathbb{H}^{H \times W}$, $\dot{\mathbf{Y}}_3 \in \mathbb{H}^{H \times r}$ and $\dot{\mathbf{Y}}_4 \in \mathbb{H}^{r \times W}$ are the quaternion Lagrangian multipliers. $\dot{\mathbf{J}} \in \mathbb{H}^{H \times r}$ and $\dot{\mathbf{P}} \in \mathbb{H}^{r \times W}$ are the adjoint variables to replace $\dot{\mathbf{A}}$ and $\dot{\mathbf{B}}$. In addition, μ_1 and μ_2 are penalty factors. The final solution can be gained by alternately updating variables. However, too many unknown variables are coupled in Eq. (10). This evidently increases the computational complexity of the proposed model, and even results in the loss of the solution. For this reason, we left out the decomposition process temporarily, but first found the lighting suppression process for solving $\dot{\mathbf{I}}$ and $\dot{\mathbf{G}}$ [17].

Update $\dot{\mathbf{I}}$. Fix $\dot{\mathbf{G}}$ and $\dot{\mathbf{Y}}_5$. The subproblem of $\dot{\mathbf{I}}$ can be solved using quaternion fast Fourier transform $\mathcal{F}(\cdot)$ under the quaternion periodic boundary condition [28].

$$\dot{\mathbf{I}} = \mathcal{F}^{-1} \left(\frac{\mathcal{F}(2\lambda \Delta^H \Delta) \cdot \mathcal{F}(\dot{\mathbf{L}}) + \mu \mathcal{F}(\text{conj}(\nabla)) \mathcal{F}(\dot{\mathbf{G}})}{\mathcal{F}(\mu \nabla^H \nabla + 2\lambda \Delta^H \Delta) + \text{eps}} \right). \quad (11)$$

Update $\dot{\mathbf{G}}$. Fix $\dot{\mathbf{I}}$ and $\dot{\mathbf{Y}}_5$. The $\dot{\mathbf{G}}$'s subproblem can be solved using Lemma 4.

Lemma 4. (Quaternion soft-thresholding operator [27]) Let $\dot{\mathbf{X}} \in \mathbb{H}$ to find the optimal solution of the problem

$$\begin{aligned} \dot{\mathbf{X}} = \arg \min_{\dot{\mathbf{X}}} & \tau \|\dot{\mathbf{X}}\|_1 + \frac{1}{2} \|\dot{\mathbf{X}} - \dot{\mathbf{Y}}\|_F^2 \\ \dot{\mathbf{X}}(:, i) = & \begin{cases} \frac{\|\dot{\mathbf{Y}}(:, i)\|_1 - \tau}{\|\dot{\mathbf{Y}}(:, i)\|_1} \dot{\mathbf{Y}}(:, i), & \|\dot{\mathbf{Y}}(:, i)\|_1 > \tau \\ 0, & \text{otherwise} \end{cases} \end{aligned} \quad (12)$$

Update $\dot{\mathbf{A}}$. Fix $\dot{\mathbf{B}}$, $\dot{\mathbf{Z}}$, $\dot{\mathbf{J}}$, $\dot{\mathbf{Y}}_2$ and $\dot{\mathbf{Y}}_3$, and let the derivatives of \mathcal{L} with respect to $\dot{\mathbf{A}}$ equal to zero. Let $\dot{\mathbf{R}}_1$ be equal to $(\dot{\mathbf{Z}} + \frac{\dot{\mathbf{Y}}_2}{\mu})\dot{\mathbf{B}}^H + \dot{\mathbf{J}} - \frac{\dot{\mathbf{Y}}_3}{\mu}$. The closed-form solution is obtained in $\dot{\mathbf{A}}$'s subproblem of Eq. (13).

$$\dot{\mathbf{A}} = \dot{\mathbf{R}}_1 (\dot{\mathbf{B}}\dot{\mathbf{B}}^H + \dot{\mathbf{I}}_d)^{-1}. \quad (13)$$

Update $\dot{\mathbf{B}}$. Similar to $\dot{\mathbf{A}}$'s optimization process, let the derivatives of \mathcal{L} with respect to $\dot{\mathbf{B}}$ equal to zero. Let $\dot{\mathbf{R}}_2$ be equal to $\dot{\mathbf{A}}^H (\dot{\mathbf{Z}} + \frac{\dot{\mathbf{Y}}_2}{\mu}) + \dot{\mathbf{P}} - \frac{\dot{\mathbf{Y}}_4}{\mu}$. The closed-form solution is obtained in $\dot{\mathbf{B}}$'s subproblem of Eq. (14).

$$\dot{\mathbf{B}} = (\dot{\mathbf{A}}^H \dot{\mathbf{A}} + \dot{\mathbf{I}}_d)^{-1} (\dot{\mathbf{R}}_2). \quad (14)$$

Update $\dot{\mathbf{Z}}$. Fix $\dot{\mathbf{D}}$, $\dot{\mathbf{E}}$, $\dot{\mathbf{Y}}_1$ and $\dot{\mathbf{Y}}_2$, and let the derivatives of \mathcal{L} with respect to $\dot{\mathbf{Z}}$ equal to zero. $\dot{\mathbf{Z}}$ can be updated below:

$$\dot{\mathbf{Z}} = (\dot{\mathbf{I}} - \dot{\mathbf{D}} - \dot{\mathbf{E}} + \frac{\dot{\mathbf{Y}}_1}{\mu} + \dot{\mathbf{A}}\dot{\mathbf{B}} - \frac{\dot{\mathbf{Y}}_2}{\mu})/2. \quad (15)$$

Update $\dot{\mathbf{J}}$ and $\dot{\mathbf{P}}$. Fix $\dot{\mathbf{A}}$, $\dot{\mathbf{B}}$, $\dot{\mathbf{Y}}_3$ and $\dot{\mathbf{Y}}_4$, $\dot{\mathbf{J}}$ and $\dot{\mathbf{P}}$ are solved using Lemma 1 and 2. The details are found in the supplementary material.

Update $\dot{\mathbf{D}}$. Fix $\dot{\mathbf{Z}}$, $\dot{\mathbf{E}}$ and $\dot{\mathbf{Y}}_1$, the $\dot{\mathbf{D}}$'s subproblem can be solved using Lemma 4.

Update $\dot{\mathbf{E}}$. Fix $\dot{\mathbf{Z}}$, $\dot{\mathbf{D}}$ and $\dot{\mathbf{Y}}_1$, the $\dot{\mathbf{E}}$'s subproblem can be solved in a closed form as below:

$$\dot{\mathbf{E}} = \mu(\dot{\mathbf{I}} - \dot{\mathbf{Z}} - \dot{\mathbf{D}})/(2\lambda + \mu). \quad (16)$$

More details of optimization process are provided in Algorithm 1.

Algorithm 1: Quaternion low-visibility feature learning

Input: The quaternion representation of the input image $\dot{\mathbf{L}}$, the parameters μ_1 , μ_2 , α , and β .
Output: Optimal lighting suppressed quaternion representation $\dot{\mathbf{I}}$ and quaternion target layer $\dot{\mathbf{D}}$

- 1 Initialize $\dot{\mathbf{G}}^0$, $\dot{\mathbf{J}}^0$, $\dot{\mathbf{P}}^0$, $\dot{\mathbf{Z}}^0$, $\dot{\mathbf{A}}^0$, $\dot{\mathbf{B}}^0$, $\dot{\mathbf{D}}^0$, $\dot{\mathbf{E}}^0$, $\dot{\mathbf{Y}}_1^0$, $\dot{\mathbf{Y}}_2^0$, $\dot{\mathbf{Y}}_3^0$, $\dot{\mathbf{Y}}_4^0$ and $\dot{\mathbf{Y}}_5^0$;
- 2 **while** not converged **do**
- 3 Fix other parameters and compute $\dot{\mathbf{I}}^t$ using Eq. (11);
- 4 Fix other parameters and compute $\dot{\mathbf{G}}^t$ using Lemma 4;
- 5 Update $\dot{\mathbf{Y}}_5^{t+1} = \dot{\mathbf{Y}}_5^t + \mu_2(\dot{\mathbf{G}}^t - H(\nabla \dot{\mathbf{I}}^t))$;
- 6 $\mu_2 = \min\{10^6, \mu_2 * 5\}$;
- 7 **end**
- 8 Perform a normalization step to bring the illumination of $\dot{\mathbf{I}}$ to a meaningful range.
- 9 **while** not converged **do**
- 10 Fix other parameters and compute $\dot{\mathbf{A}}^t$ using Eq. (13);
- 11 Fix other parameters and compute $\dot{\mathbf{B}}^t$ using Eq. (14);
- 12 Fix other parameters and compute $\dot{\mathbf{Z}}^t$ using Eq. (15);
- 13 Fix other parameters and compute $\dot{\mathbf{J}}^t$ using lemma 1 and 2;
- 14 Fix other parameters and compute $\dot{\mathbf{P}}^t$ using lemma 1 and 2;
- 15 Fix other parameters and solve $\dot{\mathbf{D}}^t$ using lemma 4;
- 16 Fix other parameters and solve $\dot{\mathbf{E}}^t$ using Eq. (16);
- 17 Update $\dot{\mathbf{Y}}_1^{t+1} = \dot{\mathbf{Y}}_1^t + \mu_1(\dot{\mathbf{I}}^t - \dot{\mathbf{Z}}^t - \dot{\mathbf{D}}^t - \dot{\mathbf{E}}^t)$;
- 18 Update $\dot{\mathbf{Y}}_2^{t+1} = \dot{\mathbf{Y}}_2^t + \mu_1(\dot{\mathbf{Z}}^t - \dot{\mathbf{A}}^t\dot{\mathbf{B}}^t)$;
- 19 Update $\dot{\mathbf{Y}}_3^{t+1} = \dot{\mathbf{Y}}_3^t + \mu_1(\dot{\mathbf{A}}^t - \dot{\mathbf{J}}^t)$;
- 20 Update $\dot{\mathbf{Y}}_4^{t+1} = \dot{\mathbf{Y}}_4^t + \mu_1(\dot{\mathbf{B}}^t - \dot{\mathbf{P}}^t)$;
- 21 $\mu_1 = \min\{10^6, \mu_1 * 1.1\}$;
- 22 **end**

C. Quaternion adaptive unsharp masking

The proposed quaternion adaptive unsharp masking (QAUM) method is to further enhance the image details and target saliency information and reconstruct a high-quality visible quaternion representation.

Given the infrared $\mathbf{L}_f \in \mathbb{R}^{H \times W}$ and the visible \mathbf{L}_v images $\in \mathbb{R}^{H \times W \times 3}$, the quaternion representations of these two inputs can be denoted as $\dot{\mathbf{L}}_f$ and $\dot{\mathbf{L}}_v$. After the quaternion low-visibility feature learning processes for the above quaternion representations, we have the lighting suppressed quaternion representations $\dot{\mathbf{I}}_f$ and $\dot{\mathbf{I}}_v$ and quaternion salient features $\dot{\mathbf{D}}_f$ and $\dot{\mathbf{D}}_v$. The entire enhancement process in the quaternion domain for $\dot{\mathbf{I}}_v$ can be mathematically described as

$$\dot{\mathbf{I}}_{ve} = \dot{\mathbf{I}}_v + \mathbf{\Lambda}_1 \odot \dot{\mathbf{D}}_f + \mathbf{\Lambda}_2 \odot \dot{\mathbf{D}}_v \quad (17)$$

where $\dot{\mathbf{I}}_{ve}$ is the enhanced visible quaternion representation, $\mathbf{\Lambda}_1$ and $\mathbf{\Lambda}_2$ are adaptive scaling factor matrices unlike many existing unsharp masking algorithms that employ a fixed scaling factor for all pixels. Eq. (17) is used in our approach to scale $\dot{\mathbf{I}}_v$ through a pixel-wise multiplication.

We consider the scaling factor at each pixel to be computed based on the pixel intensity and saliency information of the corresponding lighting-suppressed quaternion representation. The larger the intensity or saliency value, the larger the scaling factor to be imposed. Therefore, we construct detail-enhanced quaternion representation $\dot{\mathbf{I}}_v \in \mathbb{H}^{H \times W}$ by extracting quaternion salient and illumination feature layers $\dot{\mathbf{D}}_1$ and $\dot{\mathbf{D}}_2$ from corresponding lighting suppressed quaternion representations. Here, we use a component-wise summation strategy to completely preserve the detail information of infrared-visible quaternion representations.

$$\dot{\mathbf{I}}_{ve} = \dot{\mathbf{I}}_v + \dot{\mathbf{D}}_1 + \dot{\mathbf{D}}_2 \quad (18)$$

D. Quaternion Hierarchical Bayesian fusion

A quaternion hierarchical Bayesian fusion (QHBF) model for infrared and visible image fusion is a probabilistic framework designed to integrate complementary information from IR and VIS images into a single fused image, leveraging Bayesian inference to model uncertainties, prior knowledge, and dependencies across different levels of abstraction. The objective function is formulated as:

$$\begin{aligned} \arg \min_{\dot{\mathbf{F}}} \quad & \|\dot{\mathbf{F}} - \dot{\mathbf{I}}_v\|_1 + \phi \|\dot{\mathbf{F}} - \dot{\mathbf{I}}_f\|_1 + \frac{1}{2} w_1 \|\nabla \dot{\mathbf{F}} - \nabla \dot{\mathbf{I}}_v\|_F^2 \\ & + \frac{1}{2} w_2 \|\nabla \dot{\mathbf{F}} - \nabla \dot{\mathbf{I}}_f\|_F^2, \end{aligned} \quad (19)$$

where ϕ , w_1 and w_2 are real-valued parameters. We simply substitute the two fidelity terms by letting $\dot{\mathbf{S}} = \dot{\mathbf{F}} - \dot{\mathbf{I}}_v$, $\dot{\mathbf{T}} = \dot{\mathbf{I}}_f - \dot{\mathbf{I}}_v$ where $\dot{\mathbf{T}}$ is known. Thus, we have

$$\arg \min_{\dot{\mathbf{S}}} \quad \|\dot{\mathbf{S}}\|_1 + \phi \|\dot{\mathbf{T}} - \dot{\mathbf{S}}\|_1, \quad (20)$$

We formulate a regression problem: $\dot{\mathbf{T}} = \dot{\mathbf{S}} + \dot{\mathbf{Q}}$ where $\dot{\mathbf{S}}$ and corresponding noise $\dot{\mathbf{Q}}$ are governed by Laplacian distribution.

We can obtain the condition distribution of $\dot{\mathbf{Q}}$ denoted as L_q and the distribution of $\dot{\mathbf{S}}$ denoted as L_s :

$$\begin{aligned} L_q &= \prod_{i,j} \frac{1}{2\epsilon_q} \exp\left(-\frac{|\dot{q}_{i,j}|}{\epsilon_q}\right) \\ L_s &= \prod_{i,j} \frac{1}{2\epsilon_s} \exp\left(-\frac{|\dot{s}_{i,j}|}{\epsilon_s}\right), \end{aligned} \quad (21)$$

where ϵ_s and ϵ_q are scale parameters. Inspired by [34], we can transform the distributions of L_q and L_s in a hierarchical Bayesian manner:

$$\begin{cases} |\dot{q}_{i,j}| \mid n_{i,j} \sim \mathcal{N}(|\dot{q}_{i,j}| \mid 0, n_{i,j}) \\ n_{i,j} \sim \mathcal{E}\mathcal{X}\mathcal{P}(n_{i,j}, \epsilon_q) \\ |\dot{s}_{i,j}| \mid m_{i,j} \sim \mathcal{N}(|\dot{s}_{i,j}| \mid 0, m_{i,j}) \\ m_{i,j} \sim \mathcal{E}\mathcal{X}\mathcal{P}(m_{i,j}, \epsilon_s) \end{cases} \quad (22)$$

where $\mathcal{N}(\cdot)$ and $\mathcal{E}\mathcal{X}\mathcal{P}(\cdot)$ are Gaussian and exponential distributions respectively.

With the gradient regularization terms of Eq. (19), the objective function is totally substituted with $\dot{\mathbf{S}}$ and $\dot{\mathbf{T}}$ and rewritten as

$$\arg \min_{\dot{\mathbf{S}}} \quad \|\dot{\mathbf{S}}\|_1 + \phi \|\dot{\mathbf{Q}}\|_1 + \frac{1}{2} w_1 \|\nabla \dot{\mathbf{S}}\|_F^2 + \frac{1}{2} w_2 \|\nabla \dot{\mathbf{Q}}\|_F^2 \quad (23)$$

The log likelihood of Eq. (23) is defined as

$$\begin{aligned} \mathcal{L}(\dot{\mathbf{S}}) &= - \sum_{i,j} \left[\frac{|\dot{s}_{i,j}|^2}{2m_{i,j}} + \frac{|\dot{q}_{i,j}|^2}{2n_{i,j}} \right] \\ &\quad - \frac{1}{2} w_1 \|\nabla \dot{\mathbf{S}}\|_F^2 - \frac{1}{2} w_2 \|\nabla \dot{\mathbf{Q}}\|_F^2 \end{aligned} \quad (24)$$

In this way, we transform the objective function with quaternion variables into a maximum likelihood problem of a probability model without parameter ϕ .

To solve the problem of Eq. (24), we adopt the *Expectation-Maximization* (EM) algorithm [35] to obtain the optimal $\dot{\mathbf{S}}$. In E-step, we formulate an expectation of log likelihood function, called the Q -function using the variables estimated in the t^{th} iteration.

$$Q(|\dot{\mathbf{S}}| \mid |\dot{\mathbf{S}}|^{(t)}) = \mathbb{E}_{M,N|\dot{\mathbf{S}}^{(t)}, \dot{\mathbf{Q}}}[\mathcal{L}(\dot{\mathbf{S}})] \quad (25)$$

In M-step, we find $\dot{\mathbf{S}}$ corresponding to the max Q -function. We will show the optimization details of each step.

E-step. We have the expectation of the variables $\frac{1}{m_{i,j}}$ and $\frac{1}{n_{i,j}}$:

$$\begin{aligned} \mathbb{E}_{m_{i,j}|\dot{s}_{i,j}|^{(t)}} \left[\frac{1}{m_{i,j}} \right] &= \sqrt{\frac{2|\dot{s}_{i,j}|^{(t)2}}{\epsilon_s}} \\ \mathbb{E}_{n_{i,j}|\dot{q}_{i,j}|^{(t)}} \left[\frac{1}{n_{i,j}} \right] &= \sqrt{\frac{2|\dot{q}_{i,j}|^{(t)2}}{\epsilon_q}} \end{aligned} \quad (26)$$

To prove it, we set $\tilde{m}_{i,j} = \frac{1}{m_{i,j}}$ and $\tilde{n}_{i,j} = \frac{1}{n_{i,j}}$. Bayes' theorem gives

$$\begin{aligned} p(\tilde{m}_{i,j} \mid |\dot{s}_{i,j}|) &\propto p(|\dot{s}_{i,j}|, \tilde{m}_{i,j}) p(\tilde{m}_{i,j}) \\ &\propto \tilde{m}_{i,j}^{-3/2} \exp\left[-\frac{1}{2}(|\dot{s}_{i,j}|^2 \tilde{m}_{i,j} + \frac{2}{\tilde{m}_{i,j} \epsilon_s})\right] \end{aligned} \quad (27)$$

Therefore, we have

$$p(\tilde{m}_{i,j} | |\dot{s}_{i,j}|) = \mathcal{N}(\tilde{m}_{i,j} | \sqrt{\frac{2|\dot{s}_{i,j}|^2}{\epsilon_s}}, \frac{2}{\epsilon_s})$$

where $\mathcal{N}(\cdot, \cdot)$ is the inverse Gaussian distribution. In a similar way, we have the posterior density of $\tilde{n}_{i,j}$

$$p(\tilde{n}_{i,j} | |\dot{q}_{i,j}|) = \mathcal{N}(\tilde{n}_{i,j} | \sqrt{\frac{2|\dot{q}_{i,j}|^2}{\epsilon_q}}, \frac{2}{\epsilon_q})$$

Finally, the conditional expectation of $\frac{1}{m_{i,j}}$ and $\frac{1}{n_{i,j}}$ are the mean parameters of the corresponding inverse Gaussian distribution respectively.

M-step. The negative Q -function is minimized and the corresponding objective function is formulated as

$$\arg \min_{\dot{\mathbf{S}}, \dot{\mathbf{Q}}} \|\mathbf{M} \odot \dot{\mathbf{S}}\|_F^2 + \|\mathbf{N} \odot \dot{\mathbf{Q}}\|_F^2 + \frac{1}{2} w_1 \|\nabla \dot{\mathbf{S}}\|_F^2 + \frac{1}{2} w_2 \|\nabla \dot{\mathbf{Q}}\|_F^2, \quad (28)$$

where \mathbf{M} and \mathbf{N} are real-valued matrices with each element being $\mathbb{E}_{m_{i,j} | |\dot{s}_{i,j}|^{(t)}}[\frac{1}{m_{i,j}}]$ and $\mathbb{E}_{n_{i,j} | |\dot{q}_{i,j}|^{(t)}}[\frac{1}{n_{i,j}}]$. \odot denotes element-wise multiplication of two matrices. The QADMM framework [33] is employed to solve this problem. And the hyperparameters ϵ_s and ϵ_q can be updated automatically for next iteration [14].

Finally, the final fused result $\dot{\mathbf{F}}$ is reconstructed by

$$\dot{\mathbf{F}} = \dot{\mathbf{S}} + \dot{\mathbf{I}}_v. \quad (29)$$

IV. EXPERIMENTS

To evaluate the fusion performance of our framework, we conduct experiments on four public datasets. Section A presents experimental settings like competing methods, datasets, and evaluation metrics. Section B discusses the convergence and optimal parameters of the QLVFL model. To demonstrate the superiority of our method, Section C presents experimental results compared with other state-of-the-art approaches. Section D presents ablation studies on the M3FD dataset [7] to verify the effectiveness of our QIVIF framework.

A. Experimental settings

In our experimental settings, the stopping criterion of the QLVFL model is set to $1e-5$. Additionally, all the experiments are performed on a 2.90GHz Intel Core CPU and 16GB memory using Matlab 2016 version software.

Datasets. We present five types of low-visibility scenarios, including color-shift, glow effect, haze, low-light, and overexposure, as shown in Fig. 1. These datasets are composed using publicly available IVIF data. In [36], thirteen pairs of infrared and color visible images, each with a size of 328×254 , are used in the "color-shift" dataset for IVIF tasks. In [7], twenty-two pairs of infrared and color visible images, each with a size of 1024×768 , are added to the "glow effect" dataset. Additionally, fifteen pairs of infrared and color visible images, each with a size of 1024×768 , are incorporated into the "haze" dataset. In [37], five pairs of infrared and color visible images,

each with a size of 1280×1024 , are included in the "low-light" dataset. Finally, in [38], ten pairs of infrared and color visible images, each with a size of 500×329 , are added to the "overexposure" dataset.

Metrics. As referenced in [36], six objective metrics are used to quantitatively evaluate the performance of fusion quality. These include the normalized mutual information MI , the entropy EN , the contrast-based metric SD , the gradient-based metrics AG and SF , and the Q_{abf} . MI measures the amount of shared information between the fused image and the source images (infrared and visible), evaluating how much information is preserved from both modalities. EN quantifies the randomness or uncertainty (information content) in the fused image; higher EN values generally indicate that the fused image contains more texture, complexity, and detail. SD assesses the contrast or variation in pixel intensity values of the fused image. SF measures the amount of spatial information (texture and fine details) in the image, with higher SF suggesting that the fused image has more spatial details. AG evaluates the overall gradient or edge strength in the fused image. Finally, Q_{abf} is used to assess the overall quality of the fused image with respect to both spatial and contextual factors, considering the adaptability of the fusion method and how well it balances spatial and spectral details.

Comparison methods. Seven representative infrared-visible image fusion algorithms are selected as the comparison methods, which include two traditional IVIF methods LatLRR [17] and AVSHB [14], general image fusion-based learning method SwinFusion [9], low-rank representation guided method LRR-Net [32], recent task-specific based methods MEtaFusion [39] and SHIP [12], and a degradation-aware Network DAFusion [13].

B. Convergence analysis and parameter sensitivity

The convergence analysis of the QLVFL model is provided in this subsection. Fig. 6 displays the evolution curves of the relative difference versus iterations of the QLVFL model on the samples of RoadScene [38] and M3FD dataset [7]. The relative difference is calculated using maximum value selection. As displayed in Fig. 6, QLVFL is convergent and its total number of iterations is 20. This can sufficiently guarantee convergence.

In the QLVFL model, parameters p and n control the structure features while parameters β and μ_1 handles the detail features. To quantitatively analyze the sensitivity of QLVFL versus these parameters, Fig. 7 displays the SF results of QLVFL with the samples of infrared and visible images. In Fig. 7 (a) and (b), p and β are set to 1 or 1.25 and 0.1 or 0.01 for the infrared or the visible. In Fig. 7 (c) and (d), p_1 is set to 10 for the infrared and μ_1 is set to 0.5 and 0.1 for the infrared and the visible respectively.

C. Infrared visible image fusion

Quantitative evaluation. The average performance of various algorithms across five challenging datasets is presented in Table I. A higher value indicates better performance. To effectively evaluate the objective quality of the fused images,

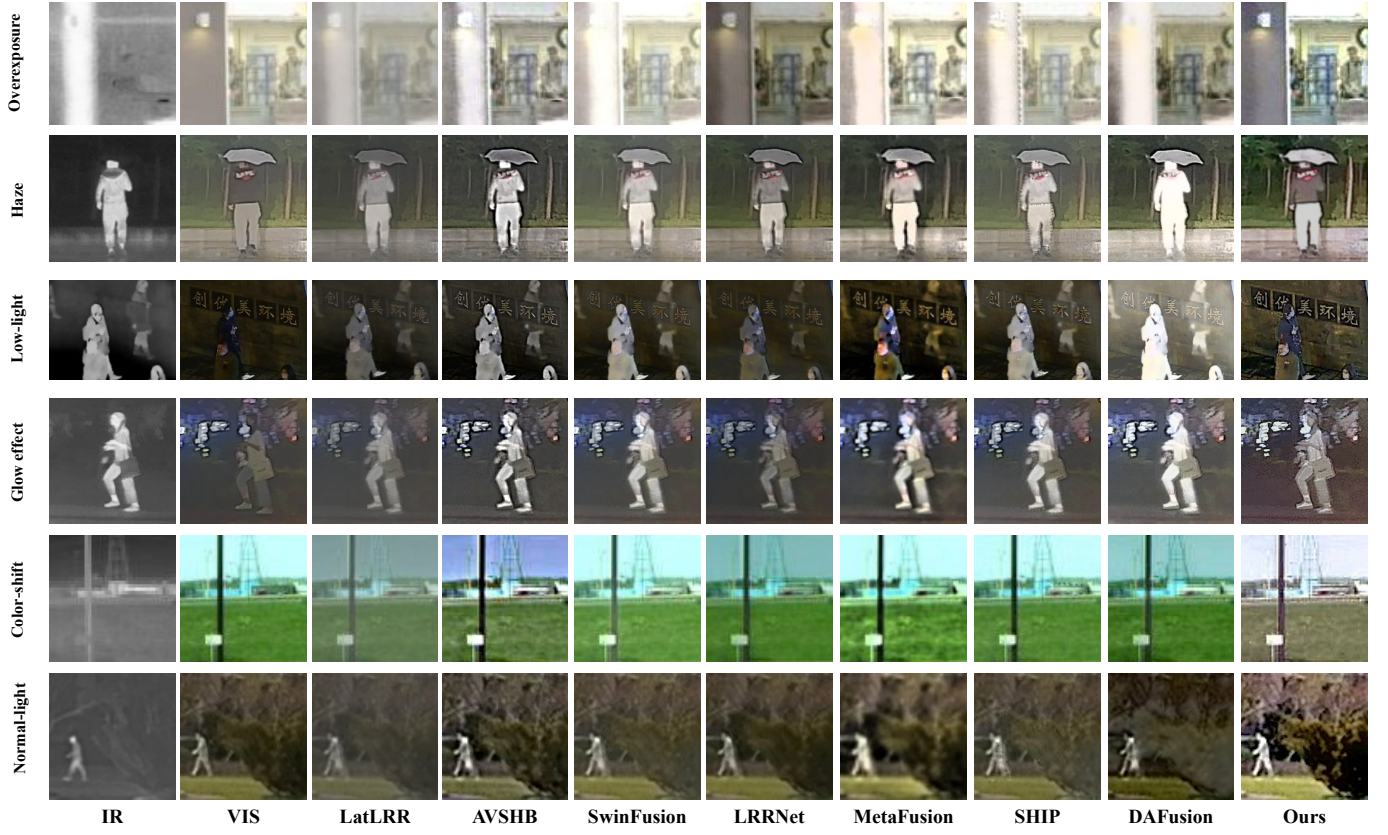


Fig. 8. Visual comparison of infrared visible image fusion results under various low-contrast conditions.



Fig. 9. The comparison of different decomposition-based methods to validate the effectiveness of detail and salient information extraction. The first row displays the various results of \hat{D} for the infrared image while the second row shows different \hat{D} for the visible image.

TABLE II
ABLATION STUDY OF OUR QIVIF FRAMEWORK (BEST RESULTS ARE IN BOLD).

Module			Metric		
QLCFL	QAUM	QHBF	$SD \uparrow$	$SF \uparrow$	$EN \uparrow$
✗	✗	✓	91.7479	0.0382	6.4328
✓	✓	✗	116.9553	0.0691	6.9091
✓	✗	✓	142.5856	0.0902	7.2394
✓	✓	✓	156.4869	0.1018	7.2797

information-based metric EN for performance evaluation. As clearly illustrated in Table II, the different settings of terms influence the fusion results to varying degrees, and the QIVIF framework yields the best quantitative results. Therefore, this experiment further validates the effectiveness of a ll the modules of QIVIF.

Effectiveness of QLVFL. To verify the advantages of



Fig. 10. Visual comparison of lighting suppression in real and quaternion domains.

the QLVFL model, we perform the ablation experiment on infrared and degraded visible images and compare various decomposition-based methods that aim to validate the effectiveness of detail and salient information extraction. The analysis of QLVFL with different model-based methods is

provided, which aims to discuss how they influence the overall feature learning performance. The first row presents the results for the infrared image, while the second row displays the results for the visible image. The models include edge-preserving-based minimization, quaternion nuclear norm minimization (QNNM), quaternion bilinear-factor nuclear norm minimization (QBNNM) [19], quaternion bilinear-factor weighted Schatten- p norm minimization (QBWSNM) [19], QLRD and QLVFL.

We can observe how each method contributes to overall fusion performance and better understand the strengths of the proposed framework in extracting and integrating relevant details as clearly illustrated in Fig. 9. Furthermore, this experiment verifies the effectiveness of quaternion lighting suppression without color casts in Fig. 10.

V. CONCLUSION

We proposed a quaternion-based infrared-visible image fusion framework that is entirely in the quaternion domain to comprehensively extract complementary features from both infrared and visible modalities. This enabled robust enhancement and fusion under various low-visibility conditions. The framework introduced a quaternion low-visibility feature learning module, which iteratively learns salient thermal targets and fine-grained texture details from both infrared and visible images in challenging conditions. To enhance the details of a degraded visible image, the framework incorporated a quaternion adaptive unsharp masking method, which injected salient and detailed information to reconstruct the visible image with balanced illumination. Additionally, a quaternion hierarchical Bayesian fusion model was proposed to integrate infrared saliency and enhanced visible details, ensuring high-visibility outputs that preserve thermal targets and maintain natural color balance. Extensive experiments across diverse datasets demonstrated that our framework outperforms state-of-the-art IVIF methods in both qualitative and quantitative metrics, particularly under challenging low-visibility conditions

REFERENCES

- [1] D. Wang, J. Liu, R. Liu, and X. Fan, "An interactively reinforced paradigm for joint infrared-visible image fusion and saliency object detection," *Information Fusion*, vol. 98, p. 101828, 2023.
- [2] H. Sun, Q. Liu, J. Wang, J. Ren, Y. Wu, H. Zhao, and H. Li, "Fusion of infrared and visible images for remote detection of low-altitude slow-speed small targets," *IEEE Journal of Selected Topics in Applied Earth Observations and Remote Sensing*, vol. 14, pp. 2971–2983, 2021.
- [3] D. Yuan, H. Zhang, X. Shu, Q. Liu, X. Chang, Z. He, and G. Shi, "Thermal infrared target tracking: A comprehensive review," *IEEE Transactions on Instrumentation and Measurement*, vol. 73, pp. 1–19, 2023.
- [4] X. Zhang, P. Ye, S. Peng, J. Liu, K. Gong, and G. Xiao, "SiamFT: An RGB-infrared fusion tracking method via fully convolutional siamese networks," *IEEE Access*, vol. 7, pp. 122 122–122 133, 2019.
- [5] S. Li, L. Fei, B. Zhang, X. Ning, and L. Wu, "Hand-based multimodal biometric fusion: A review," *Information Fusion*, p. 102418, 2024.
- [6] S. M. Z. Z. Ariffin, N. Jamil, and P. N. M. A. Rahman, "Can thermal and visible image fusion improves ear recognition?" in *2017 8th International Conference on Information Technology (ICIT)*. IEEE, 2017, pp. 780–784.
- [7] J. Liu, X. Fan, Z. Huang, G. Wu, R. Liu, W. Zhong, and Z. Luo, "Target-aware dual adversarial learning and a multi-scenario multi-modality benchmark to fuse infrared and visible for object detection," in *Proceedings of the IEEE/CVF Conference on Computer Vision and Pattern Recognition*, 2022, pp. 5802–5811.
- [8] Y. Yang, J. Liu, S. Huang, W. Wan, W. Wen, and J. Guan, "Infrared and visible image fusion via texture conditional generative adversarial network," *IEEE Transactions on Circuits and Systems for Video Technology*, vol. 31, no. 12, pp. 4771–4783, 2021.
- [9] J. Ma, L. Tang, F. Fan, J. Huang, X. Mei, and Y. Ma, "SwinFusion: Cross-domain long-range learning for general image fusion via swin transformer," *IEEE/CAA Journal of Automatica Sinica*, vol. 9, no. 7, pp. 1200–1217, 2022.
- [10] J. Yue, L. Fang, S. Xia, Y. Deng, and J. Ma, "Dif-fusion: Toward high color fidelity in infrared and visible image fusion with diffusion models," *IEEE Transactions on Image Processing*, vol. 32, pp. 5705–5720, 2023.
- [11] L. Tang, X. Xiang, H. Zhang, M. Gong, and J. Ma, "DIVFusion: Darkness-free infrared and visible image fusion," *Information Fusion*, vol. 91, pp. 477–493, 2023.
- [12] N. Zheng, M. Zhou, J. Huang, J. Hou, H. Li, Y. Xu, and F. Zhao, "Probing synergistic high-order interaction in infrared and visible image fusion," in *Proceedings of the IEEE/CVF Conference on Computer Vision and Pattern Recognition*, 2024, pp. 26 384–26 395.
- [13] X. Wang, Z. Guan, W. Qian, J. Cao, R. Ma, and C. Bi, "A degradation-aware guided fusion network for infrared and visible image," *Information Fusion*, vol. 118, p. 102931, 2025.
- [14] S. Fu, R. Zheng, and X. Chen, "Adaptive infrared and visible image fusion based on visual saliency and hierarchical bayesian," *IEEE Transactions on Instrumentation and Measurement*, vol. 71, pp. 1–16, 2022.
- [15] H. Tang, G. Liu, Y. Qian, J. Wang, and J. Xiong, "EgeFusion: Towards edge gradient enhancement in infrared and visible image fusion with multi-scale transform," *IEEE Transactions on Computational Imaging*, vol. 10, pp. 385–398, 2024.
- [16] L. Yu, Y. Xu, H. Xu, and H. Zhang, "Quaternion-based sparse representation of color image," in *2013 IEEE International Conference on Multimedia and Expo (ICME)*. IEEE, 2013, pp. 1–7.
- [17] B. Wang, H. Niu, J. Zeng, G. Bai, S. Lin, and Y. Wang, "Latent representation learning model for multi-band images fusion via low-rank and sparse embedding," *IEEE Transactions on Multimedia*, vol. 23, pp. 3137–3152, 2020.
- [18] H. Li, X.-J. Wu, and J. Kittler, "MDLatLRR: A novel decomposition method for infrared and visible image fusion," *IEEE Transactions on Image Processing*, vol. 29, pp. 4733–4746, 2020.
- [19] J. Miao and K. I. Kou, "Quaternion-based bilinear factor matrix norm minimization for color image inpainting," *IEEE Transactions on Signal Processing*, vol. 68, pp. 5617–5631, 2020.
- [20] Z. Jia, Y. Xiang, M. Zhao, T. Wu, and M. K. Ng, "A new cross-space total variation regularization model for color image restoration with quaternion blur operator," *IEEE Transactions on Image Processing*, 2025.
- [21] C. Huang, M. K. Ng, T. Wu, and T. Zeng, "Quaternion-based dictionary learning and saturation-value total variation regularization for color image restoration," *IEEE Transactions on Multimedia*, vol. 24, pp. 3769–3781, 2021.
- [22] J. Miao, K. I. Kou, D. Cheng, and W. Liu, "Quaternion higher-order singular value decomposition and its applications in color image processing," *Information Fusion*, vol. 92, pp. 139–153, 2023.
- [23] Y. Chen, X. Xiao, and Y. Zhou, "Low-rank quaternion approximation for color image processing," *IEEE Transactions on Image Processing*, vol. 29, pp. 1426–1439, 2019.
- [24] J. Li and Y. Zhou, "Automatic color image stitching using quaternion rank-1 alignment," in *Proceedings of the IEEE/CVF Conference on Computer Vision and Pattern Recognition*, 2022, pp. 19 720–19 729.
- [25] Z. Lin, G. Quan, H. Qu, Y. Du, and J. Zhao, "LOQUAT: Low-rank quaternion reconstruction for photon-counting ct," *IEEE Transactions on Medical Imaging*, 2024.
- [26] C. Huang, J. Li, and G. Gao, "Review of quaternion-based color image processing methods," *Mathematics*, vol. 11, no. 9, p. 2056, 2023.
- [27] X. Xiao and Y. Zhou, "Two-dimensional quaternion PCA and sparse PCA," *IEEE Transactions on Neural Networks and Learning Systems*, vol. 30, no. 7, pp. 2028–2042, 2018.
- [28] C. Huang, Z. Li, Y. Liu, T. Wu, and T. Zeng, "Quaternion-based weighted nuclear norm minimization for color image restoration," *Pattern Recognition*, vol. 128, p. 108665, 2022.
- [29] T.-H. Oh, Y.-W. Tai, J.-C. Bazin, H. Kim, and I. S. Kweon, "Partial sum minimization of singular values in robust PCA: Algorithm and applications," *IEEE Transactions on Pattern Analysis and Machine Intelligence*, vol. 38, no. 4, pp. 744–758, 2015.
- [30] K. Panetta, Y. Zhou, S. Agaian, and H. Jia, "Nonlinear unsharp masking for mammogram enhancement," *IEEE Transactions on Information Technology in Biomedicine*, vol. 15, no. 6, pp. 918–928, 2011.

- [31] Y. Li, R. T. Tan, and M. S. Brown, "Nighttime haze removal with glow and multiple light colors," in *Proceedings of the IEEE International Conference on Computer Vision*, 2015, pp. 226–234.
- [32] H. Li, T. Xu, X.-J. Wu, J. Lu, and J. Kittler, "LRRNet: A novel representation learning guided fusion network for infrared and visible images," *IEEE Transactions on Pattern Analysis and Machine Intelligence*, vol. 45, no. 9, pp. 11 040–11 052, 2023.
- [33] J. Flamant, S. Miron, and D. Brie, "A general framework for constrained convex quaternion optimization," *IEEE Transactions on Signal Processing*, vol. 70, pp. 254–267, 2021.
- [34] Z. Zhao, H. Bai, Y. Zhu, J. Zhang, S. Xu, Y. Zhang, K. Zhang, D. Meng, R. Timofte, and L. Van Gool, "DDFM: denoising diffusion model for multi-modality image fusion," in *Proceedings of the IEEE/CVF International Conference on Computer Vision*, 2023, pp. 8082–8093.
- [35] A. P. Dempster, N. M. Laird, and D. B. Rubin, "Maximum likelihood from incomplete data via the EM algorithm," *Journal of the Royal Statistical Society: Series B*, vol. 39, no. 1, pp. 1–22, 1977.
- [36] X. Zhang and Y. Demiris, "Visible and infrared image fusion using deep learning," *IEEE Transactions on Pattern Analysis and Machine Intelligence*, vol. 45, no. 8, pp. 10 535–10 554, 2023.
- [37] X. Jia, C. Zhu, M. Li, W. Tang, and W. Zhou, "LLVIP: A visible-infrared paired dataset for low-light vision," in *Proceedings of the IEEE/CVF International Conference on Computer Vision*, 2021, pp. 3496–3504.
- [38] H. Xu, J. Ma, J. Jiang, X. Guo, and H. Ling, "U2Fusion: A unified unsupervised image fusion network," *IEEE Transactions on Pattern Analysis and Machine Intelligence*, 2020.
- [39] W. Zhao, S. Xie, F. Zhao, Y. He, and H. Lu, "Metafusion: Infrared and visible image fusion via meta-feature embedding from object detection," in *Proceedings of the IEEE/CVF Conference on Computer Vision and Pattern Recognition*, 2023, pp. 13 955–13 965.